Stable switching among high-order modes in polariton condensates

Yongbao Sun, Yoseob Yoon, Saeed Khan, Li Ge, Mark Steger, Loren N. Pfeiffer, Ken West, Hakan E. Türeci, David W. Snoke, and Keith A. Nelson

Phys. Rev. B **97**, 045303 — Published 22 January 2018

DOI: 10.1103/PhysRevB.97.045303

Stable switching among high-order modes in polariton condensates

Yongbao Sun,[1] Yoseob Yoon,[1,*] Saeed Khan,[2] Li Ge,[3] Mark Steger,[4] Loren N. Pfeiffer,[2] Ken West,[2] Hakan E. Türeci,[2] David W. Snoke,[5] and Keith A. Nelson[1,†]

[1]*Department of Chemistry, Massachusetts Institute of Technology, Cambridge, MA 02139, USA*

[2]*Department of Electrical Engineering, Princeton University, Princeton, NJ 08544, USA*

[3]*Department of Engineering Science and Physics, College of Staten Island, City University of New York, Staten Island, NY 10314, USA*

[4]*National Renewable Energy Laboratory, Golden, CO 80401, USA*

[5]*Department of Physics, University of Pittsburgh, Pittsburgh, PA 15218, USA*

(Dated: October 20, 2017)

Abstract

We report multistate optical switching among high-order bouncing-ball modes ("ripples") and whispering-gallery modes ("petals") of exciton-polariton condensates in a laser-generated annular trap. By tailoring the diameter and power of the annular trap, the polariton condensate can be switched among different trapped modes, accompanied by redistribution of spatial densities and superlinear increase in the emission intensities, implying that polariton condensates in this geometry could be exploited for an all-optical multistate switch. A model based on non-Hermitian modes of the generalized Gross-Pitaevskii equation reveals that this mode switching arises from competition between pump-induced gain and in-plane polariton loss. The parameters for reproducible switching among trapped modes have been measured experimentally, giving us a phase diagram for mode switching. Taken together, the experimental result and theoretical modeling advances our fundamental understanding of the spontaneous emergence of coherence and move us toward its practical exploitation.

I. INTRODUCTION

Strong coupling between cavity photons and excitonic resonances of quantum wells (QWs) placed inside the cavity leads to the formation of new mixed eigenstates known as exciton-polaritons (hereafter simply polaritons). They behave as bosons with extremely low effective mass and overall repulsive interactions. The photonic and excitonic fractions can be varied by adjusting the relative detuning of photon and exciton resonances, typically by varying the cavity width in a wedged sample structure. This allows direct control over the polariton-polariton interaction strength, which increases with the excitonic fraction.

Polaritons provide a unique testbed for the study and manipulation of macroscopic quantum effects. Quantum phenomena such as Bose-Einstein condensation have been reported from liquid helium temperature[1–3] up to room temperature[4–7] in various systems. This not only allows the investigation of quantum phenomena at elevated temperatures in a convenient fashion, but also presents exciting opportunities to create all-optical polaritonic devices. As a consequence, great efforts have been devoted to the development of techniques for manipulating the properties of microcavity polaritons[2,8–16].

Previous experiments on Bose condensation of polaritons were usually performed with the photonic resonance close to the excitonic resonance, which resulted in highly excitonic characteristics of polaritons, namely strong interactions with each other and with the lattice. Together with short cavity lifetimes, this has limited the distance polaritons could propagate[14–17]. The development of new structures with much longer cavity photon lifetimes, from 20-30 ps[11] to well over 100 ps[18–21], has allowed the possibility of polariton propagation over macroscopic distances. This property was recently used to measure the polariton-polariton interaction strength in a region with no free excitons[22].

In the present work, we generated polaritons with high photonic fractions by choosing a region of the wedged sample with large negative cavity detuning. Their highly photonic nature allowed the polaritons to propagate coherently over long distances to form condensate states with radial extent up to 50 μm inside a trap formed by an annular pattern of excitation light. While interactions of polaritons in this case are not strong enough for them to thermalize into an equilibrium gas, they still play an important role. The interactions of polaritons with excitons in the pump region causes the polaritons to feel a confining potential, which in turn allows them to undergo Bose-Einstein condensation in the trap. Furthermore,

nonlinear polariton-polariton interactions result in switching and mixing among different condensate modes at high pump powers. The spatial distributions of these modes vary dramatically with very small changes of the excitation densities and patterns, but are temporally very stable as long as the excitation power is stable. This stability has allowed us to map out the phase boundaries between different modes in our optical trap. Upon state switching with increasing excitation power, the emission intensities from the condensates also increase in a superlinear fashion. The large changes not only allow us to experimentally distinguish different quantum states, but also strongly suggests the use of polaritons in all-optical multistate switching applications.

Previous works have seen in some cases the "petal" structures described here[15,17], and other works have observed the "ripple" structures described here[13,16,23] in structures with shorter polariton lifetime, but no prior work has shown how to switch between the two structures, or their intrinsic relationship. Another study[11,24] also showed similar patterns in a one-dimensional etched structure, but with multimode behavior instead of stable switching between modes, possibly due to shorter lifetimes. In Ref. [15], a channel formed by two concentric rings of excitation light was used to generate two counter-propagating condensates. We find that the same patterns can be generated without the need for a channel. This indicates that the competition between pump-induced gain and in-plane polariton loss, without the need for a confining channel, can control the petal patterns that emerge.

II. EXPERIMENTAL OBSERVATIONS: PETALS AND RIPPLES

The microcavity used in this work is a GaAs based microcavity structure grown by molecular beam epitaxy. The cavity has a large number of distributed Bragg reflector (DBR) layers that leads to cavity lifetime of 135 ps and polariton lifetime of 270 ps at resonance[19,25]. This allows polaritons to propagate over macroscopic distances of up to millimeters. The sample was thermally attached to a cold finger in an open-loop cryostat which was stabilized at 10 K. The excitation laser is a continuous-wave (CW) laser, which was modulated by an acousto-optic modulator (AOM) at 1 kHz with a duty cycle of 0.5% to prevent unwanted sample heating. The annular trap was generated by shaping the phase front of the CW laser using a high-resolution spatial light modulator (SLM). Because of the eccentricity in the pump profile, which is approximately 0.3, the diameters reported here are geometric

means of the lengths of major and minor axes of the pattern. We find that symmetry breaking direction of the pattern formation is not related to the pump eccentricity. The photoluminescence of polaritons was collected in a reflection geometry using an objective lens with a numerical aperture (NA) of 0.28, and was relay imaged to a spectrometer CCD. The energy-resolved emissions were obtained by spectrally dispersing a specific slice of either the far-field or near-field image selected by the entrance slit of the spectrometer CCD.

Annular-shaped beams with diameters ranging from 21 μm to 54 μm were used to excite the high-Q microcavity structure. The laser beam was tuned to about 140 meV above the band gap of the GaAs QW; therefore, it essentially generated free carriers, which subsequently relaxed down to exciton and polariton states. The cavity detuning was $\hbar\delta = E_{\mathrm{cav}}(k=0) - E_{\mathrm{exc}}(k=0) = -25\,\mathrm{meV}$ which corresponds to lower polaritons that are 6% excitonic and 94% photonic. Petals and ripples were formed inside the excitation annulus, with radial extent up to 50 μm. In theory, if not limited by the pump power, higher-order condensate states with length scales on the order of millimeters[19] could be realized in this high-Q microcavity structure, making them entirely visible by eye.

"Petals" as defined here are whispering-gallery modes in the annular trap, quantized in the azimuthal direction. Figure 1 shows the emission patterns from an annular trap with a diameter of 41 μm. Below the condensation threshold, polaritons remain in the vicinity of the pump region, as shown in Fig. 1(a). The asymmetry in the density distribution is largely due to inhomogeneity of the pump intensity profile. Figure 1(c) shows the momentum distribution of the polaritons below the condensation threshold. Because the photonic mode in the microcavity has an energy gradient of 11 μeV/μm along the white solid line in Fig. 1(a), there is a net flow of polariton fluid along this energy gradient, as evidenced by the accumulation of the polariton densities with in-plane wavevector components at $k_x = -1\,\mu\mathrm{m}^{-1}$ and $k_y = 1\,\mu\mathrm{m}^{-1}$ in Fig. 1(c). The cavity gradient can also be identified from the energy-resolved emission profile in Fig. 1(e) at low pump powers. In this plot, the $x = 0$ slice of Fig. 1(a) was projected onto the entrance slit of the spectrometer CCD and then spectrally dispersed. The propagation effect can also be identified in the energy-resolved k-space emission profile as a smeared dispersion, which has been reported in Ref. [18] with the same sample structure.

When the excitation density is above the condensation threshold, polaritons propagate toward the center of the trap and form the petal state inside the excitation ring. The position of the pump annulus is plotted in Fig. 1(b) as the white dashed line. The petals demonstrate

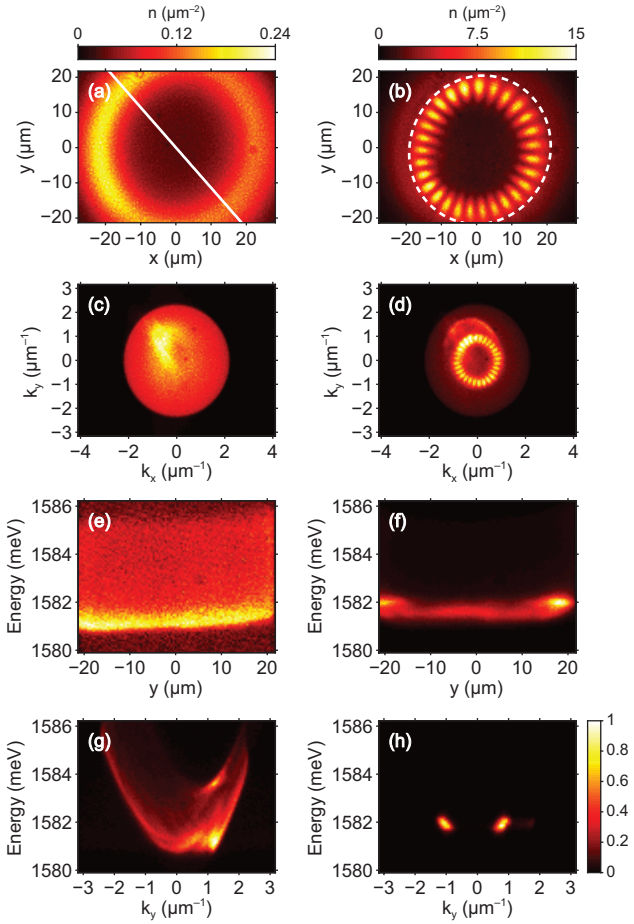

FIG. 1. Petal with 28 lobes in an annular trap with a diameter of 41 μm. (a)-(b) Polariton density distribution below (a) and above (b) condensation threshold. The white solid line in (a) indicates the direction of the cavity energy gradient (photon energy decreasing from bottom right to top left), and the white dashed line in (b) shows the position of the annular pump. (c)-(d) Polariton momentum distribution below (c) and above (d) condensation threshold. (e)-(f) Energy-resolved polariton density distribution at $x = 0$ below (e) and above (f) condensation threshold. (g)-(h) Energy-resolved polariton momentum distribution at $k_x = 0$ below (g) and above (h) condensation threshold. All results are normalized to 1 except for (a) and (b).

nodal structures similar to those of the high-order whispering-gallery modes in lasers, with the density accumulation at $k_x = -1\,\mu\text{m}^{-1}$ and $k_y = 1\,\mu\text{m}^{-1}$. The petal structure is also observed in momentum space as expected since the condensate is a coherent state and the density distributions in position space and momentum space are Fourier-transform-related. The real-space emission from the $(x, y) = (0\,\mu\text{m}, 17\,\mu\text{m})$ region, for example, corresponds

to the emission at $(k_x, k_y) = (\pm 0.83\,\mu\text{m}^{-1}, 0\,\mu\text{m}^{-1})$ in k space. The real-space distance between the lobes of the petal structure matches the period of the interference pattern given by $d = 2\pi/\Delta k = 3.8\,\mu$m. The energy-resolved measurements show narrower emission spectra from the condensates than from polaritons below the condensation threshold. Above the threshold, the energy of emission from petals is higher than emission from uncondensed polaritons that have flowed to the center of the annular trap, as seen in Fig. 1(f).

Unlike petals, "ripples" as defined here are radially confined bouncing-ball modes in the annular trap. In Fig. 2(a), we plot the emission profiles observed when an annulus with a diameter of 33 μm was used to excite the microcavity. Below the condensation threshold, the distributions of polaritons in real and momentum space show very similar signatures to those in the previous case. Confined ripples appear above the condensation threshold, as shown in Fig. 2(b). Similar patterns have been studied in quantum chaotic systems where they were termed as bouncing-ball modes[26]. In k space, we observed two large populations of polaritons at $k_x = \pm 0.73\,\mu\text{m}^{-1}$ indicative of the ripple mode, together with several states with smaller but not negligible amount of polaritons. This suggests that the ripple pattern in Fig. 2(b) can be seen as the interference of paired momentum states, where the period of the interference pattern is given by $d = 2\pi/\Delta k = 4.3\,\mu$m, matching the real-space distance between the lobes of the ripple. Figures 2(f) and (h) show energy-resolved emission along the vertical slices $x = 0$ and $k_x = 0$ in Figs. 2(b) and (d), respectively.

In this work, higher-order condensate states appear at a lower threshold than the lowest-order condensate state at $(x, y) = (0, 0)$ and $(k_x, k_y) = (0, 0)$, unlike the case in Ref. [22] where the polaritons had higher exciton fractions of 20-80%, compared to 6% in this work. In that case the balance among stronger interactions, slower transport, and longer lifetimes favors the lowest-order spatial profile. In the present work, the balance between polariton leakage from the pump region and polariton gain from the reservoir determines whether ripples or petals will define the lowest-threshold mode; this is expanded in Section IV.

III. PHASE DIAGRAM OF CONDENSATE MODES

The condensate can be switched among various petal and ripple states by varying the pump power. In the top panel of Fig. 3, we show the integrated emission intensity in the field of view as a function of the laser pump power. The emission intensity undergoes several

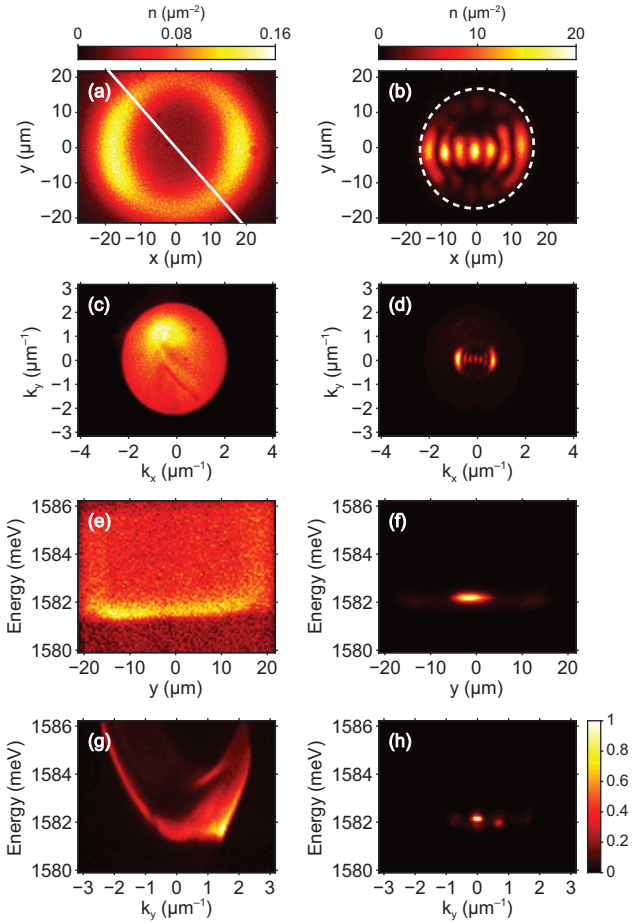

FIG. 2. Ripple with 7 lobes in an annular trap with a diameter of 33 μm. (a)-(b) Polariton density distribution below (a) and above (b) condensation threshold. The white solid line in (a) indicates the direction of the cavity energy gradient (photon energy decreasing from bottom right to top left), and the white dashed line in (b) shows the position of the annular pump. (c)-(d) Polariton momentum distribution below (c) and above (d) condensation threshold. (e)-(f) Energy-resolved polariton density distribution at $x = 0$ below (e) and above (f) condensation threshold. (g)-(h) Energy-resolved polariton momentum distribution at $k_x = 0$ below (g) and above (h) condensation threshold. All results are normalized to 1 except for (a) and (b).

distinct sharp jumps, which are marked by the red lines, and increases by five orders of magnitude when the pump power is increased by only an order of magnitude. The real-space density distributions corresponding to the green dots in the top panel are shown in Figs. 3(a)-3(f). We clearly identify that the jumps in emission intensity are accompanied by redistributions of the real-space densities, that is, by mode switching.

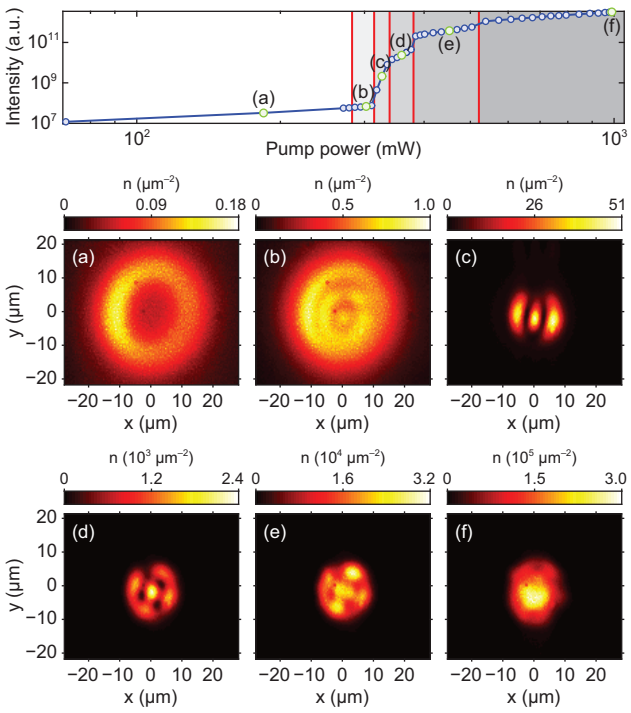

FIG. 3. Mode switching in an annular trap with a diameter of 21 μm. Top panel: the integrated emission intensity as a function of the laser pump power. Pump power at the sample is reduced to 36% of the power reported in the horizontal axis due to the overall efficiency from optics and SLM. The red lines indicate boundaries between different modes. The green circles are selected pump power levels for which the real-space density distributions of the modes are shown in (a)-(f).

In Fig. 3(a), the excitation level is below the condensation threshold, and the polariton distribution follows the excitation pattern, similar to those in Figs. 1(a) and 2(a). Figure 3(b) shows just below the onset of a higher-order state. In Fig. 3(c), a three-lobe ripple mode appears. Figures 3(d) and 3(e) show mixtures of both petals and ripples. Numerical simulations discussed below suggest that petals and ripples coexist at this power due to interactions between these states. As shown in Fig. 3(f), when the system was pumped very hard, the lowest-order condensate mode has the lowest threshold and dominantly occupied over all other modes. This power tunability of mode switching not only allows us to distinguish different high-order modes, but also suggests that polariton condensates in the annular trap can be implemented in device applications for a stable multistate switch. With finer control of the pump power and diameter, we believe more states can be accessed independently.

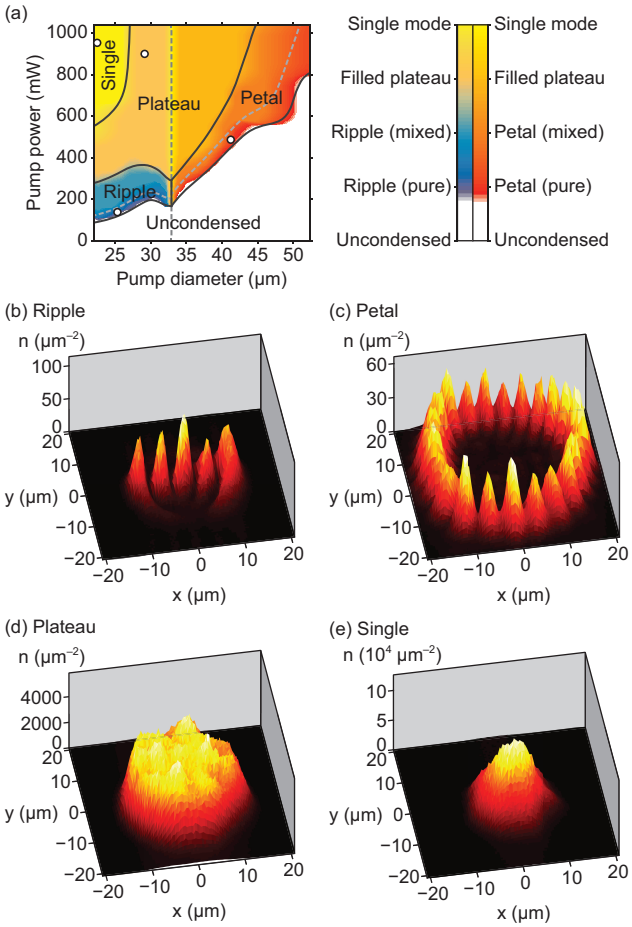

FIG. 4. (a) Phase diagram of condensate modes in an annular trap. Different colors correspond to different types of state (separated approximately by black lines, which are continuous although the data set is discrete): pure ripples are in purple, ripples mixed with petals are in blue, pure petals are in red, petals mixed with ripples are in red-orange, filled plateau states are in orange-yellow, and single mode condensate is in yellow, as depicted in the color bar. The white region represents uncondensed polaritons. The two color bars represent the two halves of the figure, separated by the vertical dashed line (the accompanying yellow line is an artifact of color averaging). Representative spatial distributions indicated by white dots in (a) are shown in (b)-(e).

In order to fully characterize the phase boundaries between different quantum states, we recorded the real-space polariton density distributions with excitation ring diameters ranging from 21 μm to 54 μm and the laser pump powers ranging from 50 mW to 1 W (18 mW to 360 mW at the sample due to the overall efficiency from optics and SLM). Because of the stability of the distributions and the superlinear increase in the emission intensities as shown

in Fig. 3, we were able to classify different quantum states at different pump conditions. The resulting phase boundaries are shown in Fig. 4(a). In this plot, different colors are assigned to different types of states with distinct spatial distributions: the white region represents uncondensed polaritons; purple and blue stand for pure ripples and ripples mixed with petals, respectively; pure petals are shown in red, while petals mixed with ripples are in red-orange; filled plateau states, where polaritons fill in the entire trap area with relatively even density distribution (but with negligible densities at and outside the pump region), are represented by the yellow-orange region. Based on our numerical simulations, mixed modes are a direct consequence of the interaction between high-order modes with very close thresholds, rather than being artifacts from time-integrated measurements. The lowest-order single-mode condensate states, coded as yellow, occupy the top left region of the phase diagram. The artificial yellow vertical line at 33 μm pump diameter is due to averaging of the different color settings [left and right color bars in Fig. 4(a)], which shows that ripple modes are favored below 33 μm, while petal modes are formed first above 33 μm. Black lines show approximate phase boundaries, which are continuous although the data set is discrete. Both petals and ripples exist in a narrow range of the phase diagram because of an abrupt increase in polariton densities within a small increase of pump power. This indicates that switching among polariton condensate states in the optical trap is very sensitive, i.e., a very low power is needed to switch between the high-order states.

Based on this phase diagram, we can identify that for a given pump power, ripples and petals will show up successively as the lowest-threshold modes by increasing the size of the ring, and the phase boundary for the lowest-threshold modes is approximately linear, both of which will be explained in the following theory section. The condensate mode can be easily tuned by changing the pump diameter and/or the pump power, as shown in Figs. 4(b)-4(e). The measured phase boundaries should serve well to calibrate the implementation of an exciton-polaritonic multistate switch by making use of the high-order quantum states.

IV. THEORY AND NUMERICAL SIMULATION OF PATTERN FORMATION

The dynamics of polariton condensate under incoherent pumping can be described using a Gross-Pitaevskii equation (GPE) for the condensate wavefunction $\Psi(\mathbf{r}, t)$, together with a dynamical equation for the density of the pump-generated exciton reservoir $n_R(\mathbf{r}, t)$, a

complex system of coupled nonlinear partial differential equations (PDEs). For pumping below threshold however, where no stable condensate mode exists, it suffices to study the GPE linearized in the condensate density; using further the steady state result for the reservoir density, this leads us to the linear dynamical equation (for details, see Appendix A):

$$\begin{aligned} i\frac{\partial \Psi}{\partial t} &= \left[-\frac{\nabla^2}{2m} + \frac{g_R}{\gamma_R} P f(\mathbf{r}) + \frac{i}{2}\left(\frac{R}{\gamma_R} P f(\mathbf{r}) - \gamma_c \right) \right] \Psi \\ &\equiv \mathcal{H}_{\mathrm{L}}(P)\Psi \end{aligned} \tag{1}$$

where $\mathcal{H}_{\mathrm{L}}(P)$ is the linear, *non-Hermitian* generator describing condensate dynamics. Its non-Hermiticity arises from polariton decay (rate γ_c) and gain through stimulated scattering from the pump-generated reservoir (rate R), while the real-valued potential represents reservoir-condensate repulsion ($\propto g_R$). P and $f(\mathbf{r})$ are, respectively, the strength (related to exciton generation rate) and spatial profile of the pump. Eigenmodes of $\mathcal{H}_{\mathrm{L}}(P)$ represent fluctuations around the uncondensed state at pump power P, and the imaginary parts of their eigenvalues describe the net polariton gain[27]. For the nth mode, beyond a power P_n its eigenvalue acquires a positive imaginary part: gain overcomes polariton loss and the fluctuations are unstable, corresponding to a condensing mode with frequency given by the real part of its eigenvalue. By varying the pump power, a set of such spatial modes $\{\varphi_n(\mathbf{r}; P_n, \omega_n)\}$ can be obtained, with linearized power thresholds $\{P_n\}$ and real frequencies $\{\omega_n\}$.

This linearization is exact until condensation first occurs, and thus the linearized mode with lowest threshold holds special significance: it is the actual mode first seen upon condensation. Naturally, the following question arises: what determines the spatial mode with lowest condensation threshold? Using a continuity equation for the condensate density derived from the GPE, it is possible to arrive at a simple formula for the linearized threshold P_n for condensation of the nth mode[28]:

$$\frac{P_n}{P_0} = \frac{1 + \gamma_n/\gamma_c}{\mathcal{G}_n} \ , \ P_0 = \frac{\gamma_c \gamma_R}{R} \tag{2}$$

where

$$\frac{\gamma_n}{\gamma_c} \propto \int_{\partial \mathcal{P}} \vec{j} \cdot d\vec{s} \ , \ \mathcal{G}_n \propto \int_{\mathcal{P}} |\varphi_n(\mathbf{r})|^2 f(\mathbf{r}) d^2\mathbf{r} \tag{3}$$

For a given mode, the threshold is determined by: (i) in-plane loss γ_n *relative* to mirror loss γ_c, the former being the flux of probability current $\vec{j}$ flowing out across the *outer* pump edge $\partial\mathcal{P}$ [see Fig. 5(a)], and (ii) $\mathcal{G}_n$, a dimensionless measure of the overlap between the mode and

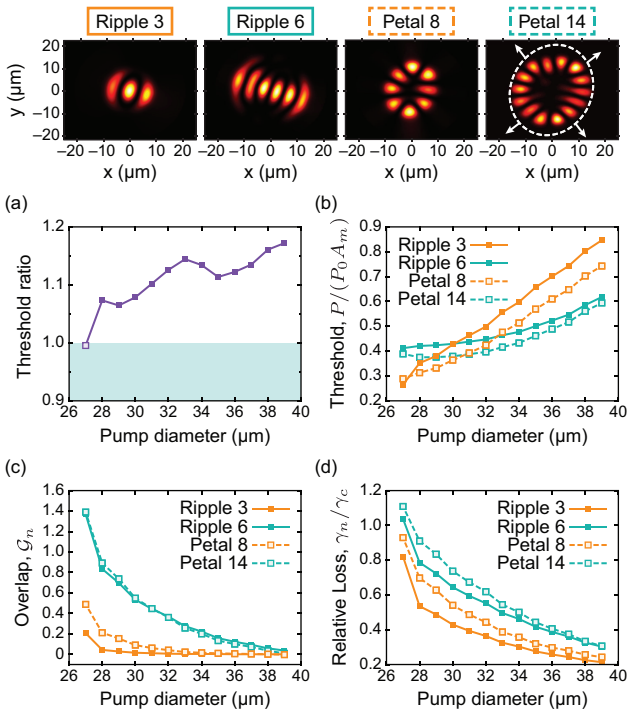

FIG. 5. (a) Ratio of power thresholds for the lowest threshold ripple mode to the lowest threshold petal mode; when the ratio is less than one (green shaded region) the ripple mode is the lowest threshold mode. Top panel: chosen linear threshold modes (petal and ripple modes), for which, as a function of pump diameter, we plot (b) linear threshold power P/P_0A_m where A_m is the area of the largest trap used in the experiment, (c) overlap $\mathcal{G}_n$, and (d) relative loss γ_n/γ_c. White dashed line in the top panel indicates the pump boundary $\partial\mathcal{P}$.

the pump within the region $\mathcal{P}$ enclosed by this pump edge. We choose $\int_{\mathcal{P}} |\varphi_n(\mathbf{r})|^2 = 1$; the resultant scaling of $\varphi_n(\mathbf{r})$ means both γ_n/γ_c and $\mathcal{G}_n$ decrease with pump size. Also, $f(\mathbf{r})$ is normalized such that $Pf(\mathbf{r})$ is the pump density in area $\mathcal{P}$. The mode with lowest threshold minimizes Eq. (2) by maximizing overlap with the pump to benefit from amplification, while still having low density near $\partial\mathcal{P}$ to reduce the relative loss. Note that for modes with smaller relative loss γ_n/γ_c, the overlap becomes more important in determining the threshold.

We study the linear modes of $\mathcal{H}_{\mathrm{L}}(P)$ for a range of pump diameters of the experimental profile. We plot of ratio of linear thresholds for the lowest threshold petal mode to the lowest order ripple mode in Fig. 5(a). Below a critical pump diameter ($\sim$28 μm in the simulation and $\sim$33 μm in the experiment), the lowest threshold mode is a ripple mode [green shaded region in Fig. 5(a)], while beyond this pump diameter, petal modes are favored for

condensation over ripple modes.

To understand this observation, we study the difference between the two types of observed condensate modes. We focus on one low order and one higher order mode of each type; these are shown in the top panel of Fig. 5. The two petal modes are labeled Petal 8 and 14, indicating the number of lobes in each mode's spatial distribution; similarly chosen ripple modes are labeled Ripple 3 and 6. For these modes, we plot their linear thresholds in Fig. 5(b), and the overlap and relative loss characteristics in Figs. 5(c) and (d) respectively, all as a function of pump diameter. We find that in general, petal modes have both stronger overlap with the pump generated reservoir, and stronger in-plane loss; this makes intuitive sense, since these modes are more localized near the pump boundary. However, we see that relative loss for all modes decreases with increase in pump diameter, as shown in Fig. 5(c); physically, this signifies that in-plane loss at the pump edge (which scales with circumference) becomes increasingly less important relative to the total mirror loss (which scales with condensate area). Due to this scaling, there exists for each mode a large enough pump diameter at which its relative loss is small, and hence where its overlap $\mathcal{G}_n$ primarily determines its threshold; in this competition, petal modes have an advantage over ripple modes.

We can now explain the transition in thresholds seen in Fig. 5(a). For small enough pump diameters, γ_n/γ_c for all petal states is large enough for them to have higher thresholds than a ripple mode, even though their pump overlap is stronger. As pump diameter increases, γ_n/γ_c decreases; at a critical pump diameter, some petal mode has low enough loss for the stronger overlap to pull its threshold down below that of the competing ripple mode. For annular profiles, a transition diameter will always exist due to the scaling of in-plane loss relative to mirror loss described earlier; the particular diameter depends on details of the profile. A similar explanation applies for higher order states: these tend to have stronger overlap but also higher relative loss, so that larger pump diameters are needed until γ_n/γ_c is small enough for the strong overlap to encourage condensation into these modes. Finally, we note that overlap $\mathcal{G}_n$ decreases as pump diameter increases [Fig. 5(b)] since the pump density $Pf(\mathbf{r})$ in region $\mathcal{P}$ goes down for a fixed annular pump width. From Eqs. (2) and (3), this decrease in $\mathcal{G}_n$ increases P_n with pump diameter; we find the simulated lowest threshold boundary is in good agreement with the experimental phase diagram [Fig. 4(a)].

Going beyond the condensation threshold, where linearization is no longer strictly valid,

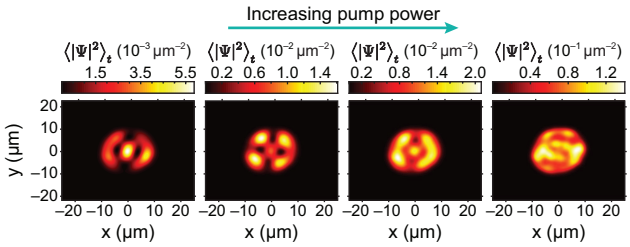

FIG. 6. Simulations including nonlinear interactions and pump depletion, based on a modal expansion of the Gross-Pitaevskii equation. Plotted is the time averaged condensate density as a function of increasing pump power from left to right. Note the different color scale in each plot, indicating increasing condensate density with pump power.

requires full simulation of the coupled nonlinear PDEs over a large spatio-temporal grid; the large condensate sizes (up to $\sim 50\,\mu$m) observed in the current work, together with polariton wavelengths ($\sim 1\,\mu$m) that demand fine spatial (and hence temporal) resolution, make such simulations very computationally expensive here. We circumvent this issue by expanding the condensate wavefunction in a pump-power-dependent, *non-Hermitian* basis, with time-dependent coefficients. Integrating out the spatial dependence then reduces the full nonlinear GPE and reservoir dynamical equation to a set of coupled ODEs, an effective nonlinear coupled mode theory for condensate and reservoir dynamics. In comparison to the usual Fourier split-step spatio-temporal integration of the GPE, this represents a substantial simplification[29]. For the choice of basis, it makes sense to use the computed linear threshold modes $\{\varphi_n(\mathbf{r}; P_n, \omega_n)\}$ that are in a quantifiable sense the preferred configurations by the polaritons for a given $f(\mathbf{r})$. We use these modes to construct a complete, biorthogonal, non-Hermitian basis set $\{\phi_n(\mathbf{r}; P)\}$ that accounts for all the spatial complexity of the *linearized* condensate problem. Applying to the specific case of a pump of diameter $26\,\mu$m, we employ this coupled mode theory and compute the time-averaged condensate density $\langle|\Psi|^2\rangle_t$. The results are plotted as a function of increasing pump power from left to right in Fig. 6. Our simulations reveal mixing of lowest threshold modes beyond threshold, when polariton-polariton interactions within the condensate become important; in particular, we reproduce qualitatively similar results to the experimentally observed coexistence of petal and ripple states shown in Fig. 3. Simulations for even the smallest pump diameter become resource intensive when many modes start interacting, with increasing pump power.

We emphasize that both the linear theory and its predicted transition diameter from

ripple to petal modes, as well as the nonlinear simulations depend on precise details of the experimental system and pump profile, as well as interaction parameters such as reservoir repulsion strength g_R and amplification rate R. Furthermore, the nonlinear theory is also found to be rather sensitive to the polariton-polariton repulsion strength and reservoir relaxation rate γ_R. Uncertainties in these quantities mean that we can only reasonably expect to capture qualitative details of the experiment, as shown here.

V. CONCLUSION AND OUTLOOK

We have seen the stable formation of high-order quantum states under non-resonant excitation, including ripples, petals, and their mixtures, with a well-defined phase diagram in the pump parameter space. Petals are whispering-gallery modes while ripples are confined bouncing-ball modes in the trap. The all-optical trapping allows facile switching among these condensate states in the annular trap, accompanied by superlinear increases in the emission intensities.

The measured patterns bear some similarity to the multiple modes seen in standard vertical-cavity surface-emitting lasers (VCSELs), e.g., the petal patterns seen in Ref. [30]. However, in typical lasers and VCSELs, the system hops uncontrollably between different modes, leading to unwanted noise (e.g., Ref. [31]). The nonlinear interactions in the polariton condensate system stabilize the modes to resist multimode behavior. This means that this system acts effectively as multistable optical switch, in which transitions between states can be controlled by small changes of the input light beam.

ACKNOWLEDGMENTS

Y.Y., Y.S. and K.A.N. were supported as part of the Center for Excitonics, an Energy Frontier Research Center funded by the US Department of Energy, Office of Science, Office of Basic Energy Sciences under Award Number DE-SC0001088, and in part by Skoltech as part of the Skoltech Next Generation Program. S.K. and H.E.T. were supported by the National Science Foundation under Grant Number DMR-1151810. L.G. was supported by CIRG 21 Grant from City University of New York. M.S. and D.W.S. were supported by the National Science Foundation under Grant Number DMR-1104383. L.N.P. and K.W. were

partially funded funded by the Gordon and Betty Moore Foundation through the EPiQS initiative Grant GBMF4420, and by the National Science Foundation MRSEC Grant DMR-1420541.

Y.Y. and Y.S. contributed equally to this work. Y.Y. and Y.S. conceived the idea. Y.Y. conducted experiments. Y.Y. and Y.S. analyzed the experimental data. S.K. and L.G. performed simulations. M.S., L.N.P., K.W. and D.W.S. designed and fabricated the sample. Y.Y., Y.S. and S.K. wrote the manuscript, with input from all authors. H.E.T., D.W.S. and K.A.N. supervised the research. All authors contributed to the analysis and discussion of the results.

Appendix A: Gross-Pitaevskii equation and linearization

We use a generalized Gross-Pitaevskii equation (GPE) to describe the dynamics of microcavity exciton-polaritons under incoherent pumping. In this standard approach[32], the nonlinear interactions of polaritons within the condensed fraction are treated at the mean-field level, while pumping and losses are introduced as complex-valued terms, so that the generalized GPE for the dynamics of the condensate wavefunction $\Psi(\mathbf{r},t)$ has the form:

$$i\frac{\partial\Psi}{\partial t} = \left[-\frac{\nabla^2}{2m} + g_R n_R + \frac{i}{2}\left(Rn_R - \gamma_c\right) + g|\Psi|^2\right]\Psi \tag{A1}$$

where for clarity we have suppressed the $(\mathbf{r},t)$ dependence of the polariton wavefunction and the density n_R of the pump-generated exciton reservoir. This reservoir gives rise to a repulsive term describing the interaction of condensate polaritons with reservoir excitons, with strength g_R, together with an amplification of the condensed fraction via stimulated scattering from the reservoir at rate R. This latter gain contribution together with the inclusion of polariton mirror loss at rate γ_c make the effective generator describing condensate dynamics non-Hermitian in this case. Finally, the polariton-polariton repulsion within the condensate appears as the nonlinear term $\propto g$ at the mean-field level. The dynamics of the pump-induced reservoir must also be accounted for by a dynamical equation of the form:

$$\frac{\partial n_R}{\partial t} = Pf(\mathbf{r}) - Rn_R|\Psi|^2 - \gamma_R n_R \tag{A2}$$

P and $f(\mathbf{r})$ are the pump strength and spatial profile as described in the main text, the source of the exciton reservoir. The aforementioned scattering from the exciton reservoir

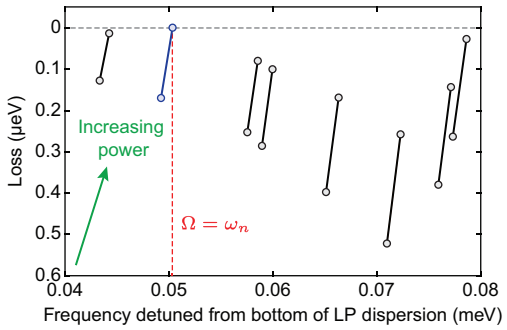

FIG. 7. Flow of (complex) eigenvalues of the linear non-Hermitian generator $\mathcal{H}_{\rm L}(P)$ as a function of pump power P across the complex plane, computed for a fixed outgoing frequency Ω. The flow direction is indicated by the arrow; eigenvalues approach the real axis from below as the pump power is increased. The lowest threshold mode is indicated in blue. It reaches the real line for the smallest pump power, *and* has a real frequency ω_n equal to the imposed outgoing frequency Ω.

into the condensate at the rate R causes a depletion of the reservoir, which is encapsulated in the second term on the right hand side. Reservoir losses that occur via mechanisms other than scattering into the reservoir (e.g. recombination losses) are described by γ_R.

For pumping below the condensation threshold, the system has a steady state with a pump generated exciton density and an uncondensed polariton state. The steady state reservoir density in this regime can be obtained after linearizing Eq. (A2) by dropping nonlinear terms of order $|\Psi|^2$; in this steady-state regime the exciton reservoir density adiabatically follows the pump:

$$n_R(\mathbf{r}, t \to \infty) = \frac{P}{\gamma_R} f(\mathbf{r}) \tag{A3}$$

Below threshold, a linearization of the GPE is also valid; we can replace $n_R(\mathbf{r}, t)$ by its linearized steady state value, and neglect the nonlinear polariton-polariton interactions $\propto g$. This yields the linearized GPE for condensate dynamics, Eq. (1) of the main text.

We now analyze steady-state condensate formation in the linearized regime. In particular, if we consider a single frequency steady-state ansätz for the condensate wavefunction:

$$\Psi(\mathbf{r}, t) = \varphi_n(\mathbf{r}) e^{-i\omega_n t}, \tag{A4}$$

the linearized GPE in Eq. (1) of the main text becomes:

$$\mathcal{H}_{\rm L}(P)\varphi_n(\mathbf{r}) = \left[-\frac{\nabla^2}{2m} + \frac{g_R}{\gamma_R} P f(\mathbf{r}) + \frac{i}{2}\frac{R}{\gamma_R} P f(\mathbf{r}) - \frac{i}{2}\gamma_c \right] \varphi_n(\mathbf{r}) = \omega_n \varphi_n(\mathbf{r}) \tag{A5}$$

The condensate wavefunction for a single frequency ω_n condensate is therefore the nth eigenmode of the generator of linearized dynamics, $\mathcal{H}_{\mathrm{L}}(P)$. We require ω_n to be a purely real frequency for the steady-state solution to correspond to a nontrivial condensate mode; we will now discuss how this requirement determines the power threshold for a given spatial mode. For simplicity, we rewrite the above eigenproblem in the form:

$$\left[-\nabla^2 + sPf(\mathbf{r})\right]\varphi_n(\mathbf{r}) = q^2\varphi_n(\mathbf{r}) \tag{A6}$$

where we have introduced the pump-induced potential s

$$\frac{s}{2m} = \frac{1}{\gamma_R}\left(g_R + \frac{i}{2}R\right) \tag{A7}$$

and the 'wavevector' $q(\omega_n)$ is defined by

$$\frac{q^2(\omega_n)}{2m} \equiv \omega_n + \frac{i}{2}\gamma_c. \tag{A8}$$

To determine the eigenmodes of $\mathcal{H}_{\mathrm{L}}(P)$, the above eigenproblem must be formulated as an appropriate boundary value problem (BVP); we make the following choice:

$$\begin{aligned}\left[-\nabla^2 + sPf(\mathbf{r})\right]\varphi_n(\mathbf{r}) &= q^2(\omega_n)\varphi_n(\mathbf{r})\ ,\ \mathbf{r}\in\mathcal{P}\\ -\nabla^2\varphi_n(\mathbf{r}) &= q^2(\omega_n)\varphi_n(\mathbf{r})\ ,\ \mathbf{r}\notin\mathcal{P}\end{aligned} \tag{A9}$$

where $\mathcal{P}$ is the region enclosed by the *outer* edge $\partial\mathcal{P}$ of the pump, as defined in the main paper. Note here that we impose an 'outgoing' boundary condition with wavevector $q(\omega_n)$ at the pump edge $\partial\mathcal{P}$, as opposed to the more usual case of considering a boundary far from the pump where the condensate wavefunction is vanishingly small and standard Dirichlet boundary conditions can be employed. For the large condensate sizes considered here, the latter approach would require simulating a very large spatial grid, making computation times inconveniently long. Our approach allows the use of a minimally relevant grid size. This occurs at a relatively minor expense: the outgoing wavevector imposed via this boundary condition depends on the unknown eigenvalue ω_n, and this BVP therefore needs to be solved self-consistently. To do so, we fix the outgoing wavevector by choosing an outgoing frequency Ω:

$$\begin{aligned}\left[-\nabla^2 + sPf(\mathbf{r})\right]\varphi_n(\mathbf{r}) &= q^2(\omega_n)\varphi_n(\mathbf{r})\ ,\ \mathbf{r}\in\mathcal{P}\\ -\nabla^2\varphi_n(\mathbf{r}) &= q^2(\Omega)\varphi_n(\mathbf{r})\ ,\ \mathbf{r}\notin\mathcal{P}.\end{aligned} \tag{A10}$$

It is now a straightforward matter to solve this BVP for a range of (increasing) values of the pump power at a fixed Ω; as a result, one obtains a set of eigenmodes $\{\varphi_n(\mathbf{r})\}$ and eigenfrequencies $\{\omega_n(P)\}$ of $\mathcal{H}_{\mathrm{L}}(P)$. These generally complex frequencies $\{\omega_n(P)\}$ flow across the complex plane as the pump-power is varied; an example of this flow is shown in Fig. 7. For a certain pump power P_n, the nth eigenfrequency ω_n crosses the real axis (becomes real). The imaginary part of ω_n represents net loss, so its becoming zero implies that gain overcomes polariton loss at this pump power, and the associated eigenmode is an unstable fluctuation around the uncondensed polariton state. Furthermore, if the (now real) frequency is *also* equal to the imposed outgoing frequency, that is $\omega_n = \Omega$, the wavevector $q(\omega_n)$ is equal both inside and outside the pump region $\mathcal{P}$. The self-consistency condition is therefore simultaneously fulfilled, and the corresponding nth eigenmode $\varphi_n(\mathbf{r};\omega_n,P_n)$ represents a true condensate mode with real frequency ω_n and *linearized* power threshold P_n. By varying the outgoing frequency Ω, and computing eigenvalues as a function of pump power, a set of such linear threshold modes $\{\varphi_n(\mathbf{r};\omega_n,P_n)\}$ can be obtained.

Appendix B: Continuity equation and linear threshold formula

From the linearized dynamical equation for the condensate wavefunction, it is possible to obtain an equation for the dynamics of the condensate *density*, $|\Psi|^2$. In particular,

$$\frac{\partial|\Psi|^2}{\partial t} = \Psi^*\frac{\partial\Psi}{\partial t} + \text{c.c.} \tag{B1}$$

From the generalized GPE [Eq. (A1)], it is easily found that:

$$\Psi^*\frac{\partial\Psi}{\partial t} = \frac{i}{2m}\Psi^*\nabla^2\Psi + \left\{-ig_R n_R - ig|\Psi|^2 + \frac{1}{2}\left(Rn_R - \gamma_c\right)\right\}|\Psi|^2 \tag{B2}$$

and so:

$$\frac{\partial|\Psi|^2}{\partial t} = \frac{i}{2m}\left(\Psi^*\nabla^2\Psi - \Psi\nabla^2\Psi^*\right) + Rn_R|\Psi|^2 - \gamma_c|\Psi|^2 \tag{B3}$$

The first term on the right hand side has the form of the divergence of a probability current; this can be made more explicit by defining the probability current $\vec{j}$ as:

$$\vec{j} = \frac{i}{2m}\left(\Psi\vec{\nabla}\Psi^* - \text{c.c.}\right) \tag{B4}$$

following which the condensate density dynamics is governed by the equation:

$$\frac{\partial|\Psi|^2}{\partial t} = Rn_R|\Psi|^2 - \nabla\cdot\vec{j} - \gamma_c|\Psi|^2 \tag{B5}$$

which has the well-defined form of a continuity equation. In particular, the above equation can be put into a more practical form by integrating over the area $\mathcal{P}$ of the region enclosed by the outer pump edge,

$$\frac{\partial}{\partial t}\int_{\mathcal{P}} d^2\mathbf{r}\ |\Psi|^2 = R\int_{\mathcal{P}} d^2\mathbf{r}\ n_R|\Psi|^2 - \oint_{\partial\mathcal{P}}\vec{j}\cdot d\vec{s} \\ - \gamma_c\int_{\mathcal{P}} d^2\mathbf{r}\ |\Psi|^2 \tag{B6}$$

where the divergence theorem allows the term involving $\vec{j}$ to be rewritten as a flux integral. This equation has the simple interpretation: any increase in the total number of polaritons ($\propto \int_{\mathcal{P}} d^2\mathbf{r}|\Psi|^2$) within the pump region comes from amplification via the exciton reservoir, at rate R. Losses to the polariton number can be attributed to either the mirror loss γ_c, or a leakage of the condensate from the pump edge. Since we are integrating within the *outer* pump edge $\partial\mathcal{P}$, beyond which by definition no source of polariton production exists, there can be no incoming probability current that would increase the polariton number within the pump region.

Now, we narrow our focus to the linearized regime, where the reservoir density $n_R = Pf(\mathbf{r})/\gamma_R$ as shown earlier. Furthermore, we consider a single mode solution such that $\Psi(\mathbf{r},t) = \varphi_n(\mathbf{r};\omega_n,P_n)e^{-i\omega_n t}$, where $\varphi_n(\mathbf{r};\omega_n,P_n)$ is the eigenmode of $\mathcal{H}_{\mathrm{L}}(P_n)$ that has (real) eigenfrequency ω_n. For simplicity, we suppress the parameters defining φ_n in what follows. With this ansätz, the condensate density is time-independent and the above continuity equation reduces to:

$$\frac{R}{\gamma_R}P\int_{\mathcal{P}} d^2\mathbf{r}f(\mathbf{r})|\varphi_n|^2 = \oint_{\partial\mathcal{P}}\vec{j}[\varphi_n]\cdot d\vec{s} + \gamma_c\int_{\mathcal{P}} d^2\mathbf{r}|\varphi_n|^2 \tag{B7}$$

Here, the probability current $\vec{j}[\varphi_n]$ is now evaluated for the eigenmode φ_n, as in the main text. Now, defining the condensate density ρ_n, pump overlap $\mathcal{G}_n$, and in-plane loss γ_n respectively as in the main paper,

$$\rho_n = \int_{\mathcal{P}} d^2\mathbf{r}\ |\varphi_n|^2 \tag{B8}$$

$$\mathcal{G}_n = \frac{1}{\rho_n}\int_{\mathcal{P}} d^2\mathbf{r}f(\mathbf{r})|\varphi_n|^2 \tag{B9}$$

$$\gamma_n = \oint_{\partial \mathcal{P}} \vec{j}[\varphi_n] \cdot d\vec{s} \tag{B10}$$

we can recover the linear threshold formula [Eq. (2) of the main text]:

$$\frac{P_n}{P_0} = \frac{1 + \gamma_n/(\rho_n \gamma_c)}{\mathcal{G}_n} \equiv \frac{1 + \Gamma_n}{\mathcal{G}_n} \tag{B11}$$

with P_n being the linear threshold power for the nth mode and $P_0 = (\gamma_c \gamma_R)/R$.

---

* yoonys@mit.edu

† kanelson@mit.edu

[1] J. Kasprzak, M. Richard, S. Kundermann, A. Baas, P. Jeambrun, J. M. J. Keeling, F. M. Marchetti, M. H. Szymańska, R. André, J. L. Staehli, V. Savona, P. B. Littlewood, B. Deveaud, and L. S. Dang, Nature **443**, 409 (2006).

[2] R. Balili, V. Hartwell, D. Snoke, L. Pfeiffer, and K. West, Science **316**, 1007 (2007).

[3] Y. Sun, P. Wen, Y. Yoon, G. Liu, M. Steger, L. N. Pfeiffer, K. West, D. W. Snoke, and K. A. Nelson, Phys. Rev. Lett. **118**, 016602 (2017).

[4] S. Christopoulos, G. Baldassarri Höger von Högersthal, A. J. D. Grundy, P. G. Lagoudakis, A. V. Kavokin, J. J. Baumberg, G. Christmann, R. Butté, E. Feltin, J.-F. Carlin, and N. Grandjean, Phys. Rev. Lett. **98**, 126405 (2007).

[5] S. Kéna-Cohen and S. R. Forrest, Nat. Photon. **4**, 371 (2010).

[6] J. D. Plumhof, T. Stöferle, L. Mai, U. Scherf, and R. F. Mahrt, Nat. Mater. **13**, 247 (2014).

[7] K. S. Daskalakis, S. A. Maier, R. Murray, and S. Kéna-Cohen, Nat. Mater. **13**, 271 (2014).

[8] R. I. Kaitouni, O. El Daïf, A. Baas, M. Richard, T. Paraiso, P. Lugan, T. Guillet, F. Morier-Genoud, J. D. Ganière, J. L. Staehli, V. Savona, and B. Deveaud, Phys. Rev. B **74**, 155311 (2006).

[9] C. W. Lai, N. Y. Kim, S. Utsunomiya, G. Roumpos, H. Deng, M. D. Fraser, T. Byrnes, P. Recher, N. Kumada, T. Fujisawa, and Y. Yamamoto, Nature **450**, 529 (2007).

[10] E. A. Cerda-Méndez, D. N. Krizhanovskii, M. Wouters, R. Bradley, K. Biermann, K. Guda, R. Hey, P. V. Santos, D. Sarkar, and M. S. Skolnick, Phys. Rev. Lett. **105**, 116402 (2010).

[11] E. Wertz, L. Ferrier, D. D. Solnyshkov, R. Johne, D. Sanvitto, A. Lemaître, I. Sagnes, R. Grousson, A. V. Kavokin, P. Senellart, G. Malpuech, and J. Bloch, Nat. Phys. **6**, 860 (2010).

[12] N. Y. Kim, K. Kusudo, C. Wu, N. Masumoto, A. Löffler, S. Höfling, N. Kumada, L. Worschech, A. Forchel, and Y. Yamamoto, Nat. Phys. **7**, 681 (2011).

[13] P. Cristofolini, A. Dreismann, G. Christmann, G. Franchetti, N. G. Berloff, P. Tsotsis, Z. Hatzopoulos, P. G. Savvidis, and J. J. Baumberg, Phys. Rev. Lett. **110**, 186403 (2013).

[14] A. Askitopoulos, H. Ohadi, A. V. Kavokin, Z. Hatzopoulos, P. G. Savvidis, and P. G. Lagoudakis, Phys. Rev. B **88**, 041308 (2013).

[15] A. Dreismann, P. Cristofolini, R. Balili, G. Christmann, F. Pinsker, N. G. Berloff, Z. Hatzopoulos, P. G. Savvidis, and J. J. Baumberg, Proc. Natl. Acad. Sci. **111**, 8770 (2014).

[16] A. Askitopoulos, T. C. H. Liew, H. Ohadi, Z. Hatzopoulos, P. G. Savvidis, and P. G. Lagoudakis, Phys. Rev. B **92**, 035305 (2015).

[17] F. Manni, K. G. Lagoudakis, T. C. H. Liew, R. André, and B. Deveaud-Plédran, Phys. Rev. Lett. **107**, 106401 (2011).

[18] B. Nelsen, G. Liu, M. Steger, D. W. Snoke, R. Balili, K. West, and L. Pfeiffer, Phys. Rev. X **3**, 041015 (2013).

[19] M. Steger, C. Gautham, D. W. Snoke, L. Pfeiffer, and K. West, Optica **2**, 1 (2015).

[20] G. Liu, D. W. Snoke, A. Daley, L. N. Pfeiffer, and K. West, Proc. Natl. Acad. Sci. **112**, 2676 (2015).

[21] D. Ballarini, D. Caputo, C. S. Muñoz, M. De Giorgi, L. Dominici, M. H. Szymańska, K. West, L. N. Pfeiffer, G. Gigli, F. P. Laussy, and D. Sanvitto, Phys. Rev. Lett. **118**, 215301 (2017).

[22] Y. Sun, Y. Yoon, M. Steger, G. Liu, L. N. Pfeiffer, K. West, D. W. Snoke, and K. A. Nelson, Nat. Phys. **13**, 870 (2017).

[23] C. Ouellet-Plamondon, G. Sallen, F. Morier-Genoud, D. Y. Oberli, M. T. Portella-Oberli, and B. Deveaud, Phys. Rev. B **93**, 085313 (2016).

[24] F. Manni, K. G. Lagoudakis, B. Pietka, L. Fontanesi, M. Wouters, V. Savona, R. André, and B. Deveaud-Plédran, Phys. Rev. Lett. **106**, 176401 (2011).

[25] M. Steger, G. Liu, B. Nelsen, C. Gautham, D. W. Snoke, R. Balili, L. Pfeiffer, and K. West, Phys. Rev. B **88**, 235314 (2013).

[26] S. W. McDonald and A. N. Kaufman, Phys. Rev. A **37**, 3067 (1988).

[27] F. Baboux, L. Ge, T. Jacqmin, M. Biondi, E. Galopin, A. Lemaître, L. Le Gratiet, I. Sagnes, S. Schmidt, H. E. Türeci, A. Amo, and J. Bloch, Phys. Rev. Lett. **116**, 066402 (2016).

[28] L. Ge, A. Nersisyan, B. Oztop, and H. E. Türeci, arXiv:1311.4847.

[29] S. Khan and H. E. Türeci, Phys. Rev. A **94**, 053856 (2016).

[30] M. Li, B. Zhang, K. P. Chen, D. W. Snoke, and A. P. Heberle, IEEE J. Quant. Electron. **48**, 1065 (2012).

[31] F. Pedaci, M. Giudici, J. R. Tredicce, and G. Giacomelli, Appl. Phys. B **81**, 993 (2005).

[32] M. Wouters and I. Carusotto, Phys. Rev. Lett. **99**, 140402 (2007).